JOURNAL OF THERMOPHYSICS AND HEAT TRANSFER
Vol. 11, No. 1, January–March 1997

Numerical Simulation of Supersonic, Chemically Reacting Flow Using an Implicit Finite Volume Method

Dieter Bohn,* Harald Schönenborn,† and Herbert Wilhelmi‡
Aachen University of Technology, Aachen 52056, Germany

The thermal design of high-loaded components of combustion chambers represents a very difficult engineering task. The aerodynamic and thermal analysis procedures currently available to designers do not allow an a priori design without expensive experimental development iterations. Numerical simulations are one possibility for reducing the experimental effort. On the one hand, codes exist for the simulation of chemically reacting flows; on the other hand, few codes exist for the coupled simulation of fluid flow and heat transfer in solid bodies. A numerical procedure for the calculation of chemically reacting flow with conjugate heat transfer in the subsonic and supersonic flow regime is presented. The numerical scheme works on the basis of an implicit finite volume method. The formulation of the governing equations in arbitrary coordinates and the use of a multiblock technique even allows the simulation of complex geometries. The code is tested using experimental data for the injection of cooling gas into a hot gas stream. The results for two different reaction schemes, a one-step global reaction scheme and a scheme involving 17 elementary reactions and nine species, demonstrate the potential of the method. Furthermore, the code is applied to the injection of hydrogen into an exhaust gas stream with the scope of film cooling with conjugate heat transfer. This approach gives more realistic results than the use of adiabatic walls.

Nomenclature

A = frequency factor, mole, cm^3, s, K
A, B, C = Jacobian matrices
D = diffusion coefficient, m^2/s
E = activation energy, kJ/mole
$\boldsymbol{E}, \boldsymbol{F}, \boldsymbol{G}$ = fluxes
e = internal energy, kJ/kg
h = enthalpy, kJ/kg
J = cell volume, m^3
k = reaction rates, mole, cm^3, s
M = blowing ratio
M = molecular weight, g/mole
n = temperature exponent
p = pressure, Pa
Q = source term
$\boldsymbol{q}$ = heat flux vector
R = universal gas constant, J/mole/K
S = source terms
T = temperature, K
t = time, s
$\boldsymbol{U}$ = vector of conservative variables
u, v, w = Cartesian velocity components, m/s
x, y, z = Cartesian coordinates, m
Y = mass fraction
γ = ratio of specific heats
η = cooling effectiveness
ξ, η, ζ = arbitrary coordinates
$\boldsymbol{\lambda}$ = heat conductivity, W/m/K
ν = stoichiometric coefficients
ρ = density, kg/m^3
τ = components of Reynolds stresses, N/m^2

Subscripts
for = formation
i = species
mix = mixture
r = real
s = sensible
∞ = freestream

Superscripts
n = time level
T = transposed

Introduction

THE thermal design of high-loaded components of combustion chambers is a very difficult engineering task. The aerodynamic and thermal analysis procedures currently available to designers do not allow an a priori design without expensive experimental development iterations. Numerical simulations are one way to reduce the experimental effort. Codes exist for the simulation of chemically reacting flows using semi-implicit finite difference[1] or finite volume methods,[2,3] or fully implicit finite volume methods.[4,5] Only a few examples of this can be given. On the other hand, few codes exist for the coupled simulation of fluid flow and heat transfer in solid bodies. NASA Langley Research Center developed a finite element code for the coupled fluid–thermal–structural analysis.[6,7] Heselhaus et al.,[8] and Heselhaus and Vogel,[9] coupled a finite volume code for fluid flow with a finite element code for heat transfer.

This article presents a numerical procedure for the coupled simulation of chemically reacting flow and heat transfer in solid bodies in just one code. The code is validated for the mixing of two species with film cooling of a flat plate and hydrogen combustion before it is applied to the simulation of hydrogen injection into an exhaust stream with the scope of film cooling. These examples show the potential of the code for the thermal design of high-loaded components.

Received Dec. 20, 1995; presented as Paper 96-0347 at the AIAA 34th Aerospace Sciences Meeting and Exhibit, Reno, NV, Jan. 15–19, 1996; revision received March 31, 1996; accepted for publication July 12, 1996.

*Professor, Director of the Institute of Steam and Gas Turbines, Templergraben 55.
†Research Engineer, Institute of Steam and Gas Turbines, Templergraben 55.
‡Professor, Institute of Industrial Furnaces, Kopernikusstrasse 16.

Governing Equations

The governing equations for the conservative variables in arbitrary, body-fitted coordinates ξ, η, and ζ with the fluxes in normal directions to the cell faces, for which ξ, η, and ζ are constant, read for the fluid flow with additional species conservation equations:

$$\boldsymbol{U}_t + \boldsymbol{E}_\xi + \boldsymbol{F}_\eta + \boldsymbol{G}_\zeta = \boldsymbol{S} \tag{1}$$

with

$$\boldsymbol{U} = J \cdot (\rho,\ \rho u,\ \rho v,\ \rho w,\ \rho e,\ \rho Y_i)^T \tag{2}$$

$$\boldsymbol{E} = J \cdot (\tilde{\boldsymbol{E}} \cdot \xi_x + \tilde{\boldsymbol{F}} \cdot \xi_y + \tilde{\boldsymbol{G}} \cdot \xi_z) \tag{3}$$

$$\tilde{\boldsymbol{E}} = \begin{matrix} \rho u \\ \rho u^2 - \tau_{xx} \\ \rho uv - \tau_{xy} \\ \rho uw - \tau_{xz} \\ (\rho e - \tau_{xx})u - \tau_{xy}v - \tau_{xz}w + q_x \\ \rho u Y_i - \rho D_i \dfrac{\partial Y_i}{\partial x} \end{matrix} \tag{4}$$

$$\boldsymbol{S} = J \cdot (0,\ 0,\ 0,\ 0,\ 0,\ W_i)^T \tag{5}$$

The fluxes $\boldsymbol{F}$ and $\boldsymbol{G}$ are obtained analogously. $\boldsymbol{q}$ contains not only the Fourier heat flux, but also the enthalpy transport by the species:

$$\boldsymbol{q} = (q_x,\ q_y,\ q_z)^T = -\boldsymbol{\lambda} \cdot \nabla T - \rho \sum_{i=0}^{N} h_i \cdot D_{i,\mathrm{mix}} \cdot \nabla Y_i \tag{6}$$

The expressions $\xi_x, \ldots$ are the metrics, which result from the coordinate transformation. The internal energy includes the heat of formation:

$$e = \sum_{i=0}^{N} Y_i \cdot \left(h_{i,\mathrm{for}} + \int_{T_{\mathrm{ref}}}^{T} c_{pi} \cdot \mathrm{d}T \right) - \frac{p}{\rho} + \frac{1}{2} \cdot (u^2 + v^2 + w^2) \tag{7}$$

For the calculation of the heat capacity and the enthalpy, data from Sandia[10] are used. The source term W_i for the chemical kinetics for every species is given by

$$W_i = M_i \cdot \sum_{r=1}^{N_r} \left\{ (\nu''_{r,i} - \nu'_{r,i}) \cdot \left[k_{f,r} \prod_{1=0}^{N} \left(\frac{\rho Y_1}{M_1} \right)^{\nu'_{r,1}} - k_{b,r} \prod_{1=0}^{N} \left(\frac{\rho Y_1}{M_1} \right)^{\nu''_{r,1}} \right] \right\} \tag{8}$$

$k_{f,r}$ and $k_{b,r}$ are the reaction rates in Arrhenius form for the forward and backward reactions:

$$k_r = A_r \cdot T^{n_r} \cdot e^{-E_r/R \cdot T} \tag{9}$$

M_i is the molecular weight of species i. For the evaluation of the reaction rates, the average temperature is used.

Mathematical Model

Making use of a Newton method leads to the following approximation of the conservation equations in implicit form:

$$\frac{\Delta \boldsymbol{U}}{\Delta t} + (A^n \cdot \Delta \boldsymbol{U})_\xi + (B^n \cdot \Delta \boldsymbol{U})_\eta + (C^n \cdot \Delta \boldsymbol{U})_\zeta + (H^n \cdot \Delta \boldsymbol{U}) = -(\boldsymbol{E}^n_\xi + \boldsymbol{F}^n_\eta + \boldsymbol{G}^n_\zeta) + \boldsymbol{S}^n \tag{10}$$

where A, B, and C are the Jacobians of the fluxes $\boldsymbol{E}$, $\boldsymbol{F}$, and $\boldsymbol{G}$, and H is the Jacobian of $\boldsymbol{S}$. The solution vector $\boldsymbol{U}^{n+1}$ at the new time level can be obtained by adding $\Delta \boldsymbol{U}$ to the old solution $\boldsymbol{U}^n$.

An upwind discretization is used for the inviscid fluxes. With respect to numerical diffusion, Godunov-type flux differencing is employed.[11] To achieve a third-order accuracy, Van Leer's MUSCL technique is used.[12] Since this Godunov flux is not sufficiently diffusive to guarantee stability in regions with complex flow phenomena, it is combined with a modified Steger–Warming flux (flux vector splitting).[13] To be able to use the old Riemann solver[14,15] developed for pure flow problems, a new energy is defined[16]:

$$(\rho e)_{\mathrm{new}} = \frac{p}{\gamma - 1} + \sum_{i=0}^{N} (\rho Y_i) \cdot h_{i,\mathrm{for}} + \rho \cdot \frac{(u^2 + v^2 + w^2)}{2} \tag{11}$$

Using the equivalent γ[4]

$$\gamma = h_{sm}/e_{sm} \tag{12}$$

with the sensible enthalpy h_{sm} of the mixture and the sensible internal energy e_{sm} (excluding the kinetic energy and heat of formation), the old internal energy can be rewritten as follows:

$$(\rho e)_{\mathrm{old}} = (\rho e)_{\mathrm{new}} + Q = (\rho e)_{\mathrm{new}} + p \cdot \left(\frac{1}{\gamma_{\mathrm{old}} - 1} - \frac{1}{\gamma - 1} \right) \tag{13}$$

Inserting this into the energy equation (here, for the sake of simplicity, only the inviscid equation in Cartesian coordinates), and putting Q as a source term on the right-hand side yields

$$(\rho e_{\mathrm{new}})_t + (Q)_t + [u \cdot (p + \rho e_{\mathrm{new}})]_x + [v \cdot (p + \rho e_{\mathrm{new}})]_y + [w \cdot (p + \rho e_{\mathrm{new}})]_z = -[(u \cdot Q)_x + (v \cdot Q)_y + (w \cdot Q)_z] \tag{14}$$

Because only a steady-state solution is calculated, the time-dependence of Q is neglected. This approach has the advantage that the old Riemann solver for the flow problem only has to be modified slightly, the pressure can always be calculated directly from the conservative flow variables, and the temperature can be obtained from the pressure using the ideal gas law without further iteration processes. The ratio γ is calculated at each iteration within the subroutines for the transport coefficients.

The viscous fluxes are approximated using central differences. The solution of the resulting system of linear equations is solved by a Gauss–Seidel point iteration scheme allowing high vectorization on present-day computers. The closure of the Favre-averaged equations is provided by the algebraic eddy–viscosity turbulence model by Baldwin and Lomax.[17] The equations have the same structure as the Reynolds-averaged equations for incompressible flow, and the turbulence model can be implemented by the usual Boussinesq approximation.

The properties of the pure species are determined on the basis of a fit of the collision integrals.[18,19] The transport coefficients of the mixture are calculated using various models. The mixture viscosity is determined by a modified Hirschfelder formulation, the mixture heat conductivity is calculated according to Hirschfelder, and the well-known model described in the Sandia National Laboratories report[10] is used for the diffusivity. The effective transport coefficients are determined using constant turbulent Prandtl and Schmidt numbers of 0.9. The transport coefficients must be accurately determined because the wall is resolved down to the viscous sublayer for the coupling procedure.

For the coupled simulations with heat transfer in solid bodies, blocks can be defined as solid-body blocks. Then, only the Fourier equation is solved in these blocks. The coupling of

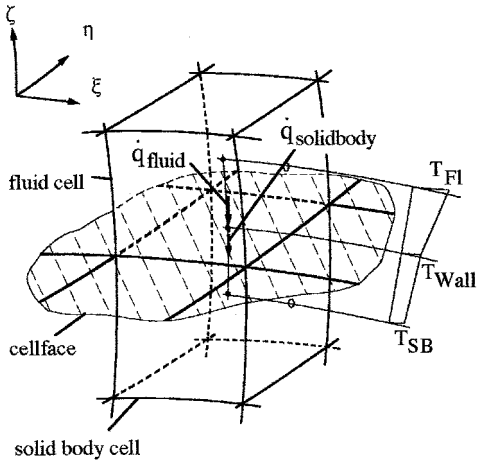

Fig. 1 Conditions at the cell face between fluid flow and solid body.

fluid blocks and solid-body blocks is achieved via a common wall temperature, resulting from the equality of the local heat fluxes passing the contacting cell faces (Fig. 1). This allows a combined simulation in just one code, without any further iteration processes. This coupling procedure has already been widely tested in turbomachinery flow.[20,21]

Results

Mixing of Two Species

As a test case for the mixing of two species, experimental data from film-cooling experiments on a flat plate were used where a coolant was injected into a hot gas stream through a slot.[22] Figure 2 shows the experimental setup in the high-enthalpy wind tunnel. The temperature and Mach number of the hot gas were varied in ranges from 1500 to 3000 K and 0.5 to 1.0, respectively. Air, helium, and argon were used as coolants. The heat flux in the wall of the flat plate was measured by pairs of thermocouples. The heat transfer through the nonadiabatic wall was taken into account by the code by means of a fully coupled simulation of fluid flow and nonadiabatic walls, as explained earlier. Figure 3 shows the computational grid for this test case. It consists of four blocks, two for the fluid flow and two for the solid bodies, with a total of 3639 grid points. The first cell center at the wall is located at a y^+ of about unity. This value is also used for the grids in the following test cases. Because this value is sufficient to guarantee good resolution of the boundary layer, no grid convergence study was performed. The other cells are distributed according to a geometric series.

Figure 4 shows a comparison between experimental data and numerical results for the temperature distribution on the top side of the flat plate downstream of the slot, which is located at $x/L = 0.14$. The measured, linearized temperature at the bottom side of the plate was used as a boundary condition for the calculations. The numerical results (at the top side) show the same tendency as the experimental data. The temperature is underestimated by about 5%. A reason for this may be the neglect of thermodiffusion, which becomes important at large temperature gradients and large differences in the molecular weight. Another reason may be the constant turbulent Schmidt number of 0.9 for the determination of the turbulent parts of the diffusivities. Libby and Williams[23] observed that for binary mixtures of gases with large differences in molar weight, the turbulent Schmidt number may be as low as 0.25. A higher diffusivity would result in a better mixing of cold and hot gas and, therefore, in a higher surface temperature. This effect is explained in further detail in the next section. However, the results can be regarded as sufficiently accurate, considering the measuring accuracy of 10%.

Hydrogen Combustion

For testing combustion, the hydrogen combustion experiment by Burrows and Kurkov[24] is simulated. The geometry of

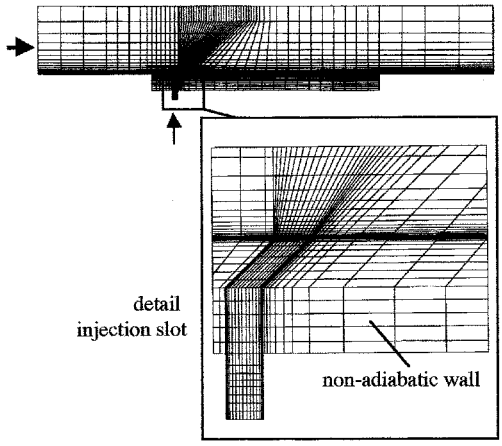

Fig. 3 Computational grid.

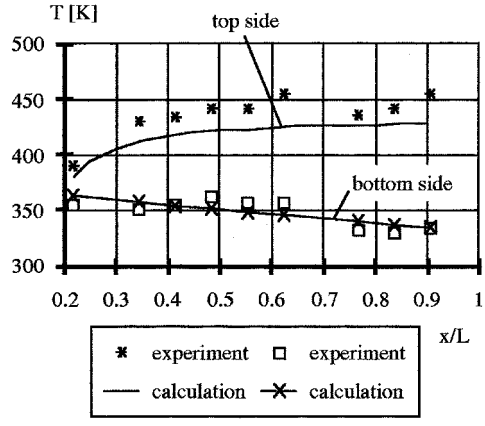

Fig. 4 Comparison between experimental data and numerical results for the film cooling of a flat plate with helium ($Ma = 0.87$, $M = 0.38$, and $Re = 2.73E+05$).

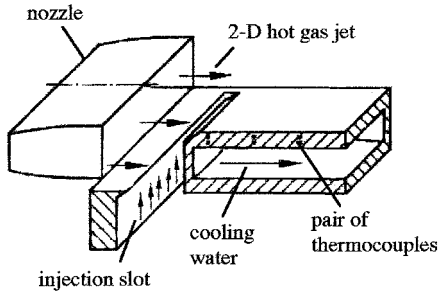

Fig. 2 High-enthalpy wind tunnel.

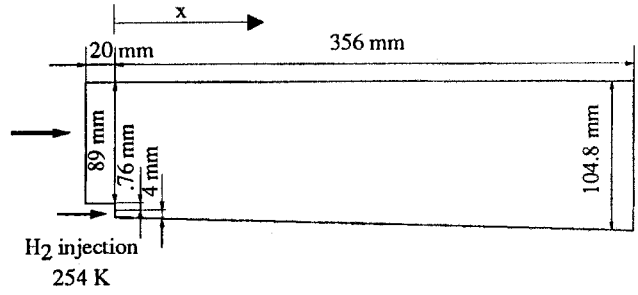

Fig. 5 Geometry for the Burrows and Kurkov[24] experiment.

the experiment is shown in Fig. 5. Hydrogen is injected sonically parallel to the wall into a supersonic airstream. The experiments were performed with and without combustion. The boundary conditions for the two test cases are listed in Table 1. A grid with two blocks and a total number of 6064 grid points is used for the numerical simulation.

Figure 6 shows the results for the mole fraction distribution at the exit plane of the channel for both the experiments and calculations. The y coordinate starts at the channel wall and is perpendicular to the x coordinate. The measurement accuracy is ±2.5%; the measurements only varied over a wider range from run to run in the reaction zone. Results for two different turbulent Schmidt numbers are shown. The solid lines represent the calculations with $Sc_t = 0.9$, and the dashed lines represent the calculations with $Sc_t = 0.25$. The overall agreement between experiments and calculations is quite satisfactory. In the vicinity of the wall, the lower Schmidt number gives the better results. As already mentioned, better mixing between the two jets takes place. More gas from the outer flow penetrates into the hydrogen stream. Figure 7 shows the corre-

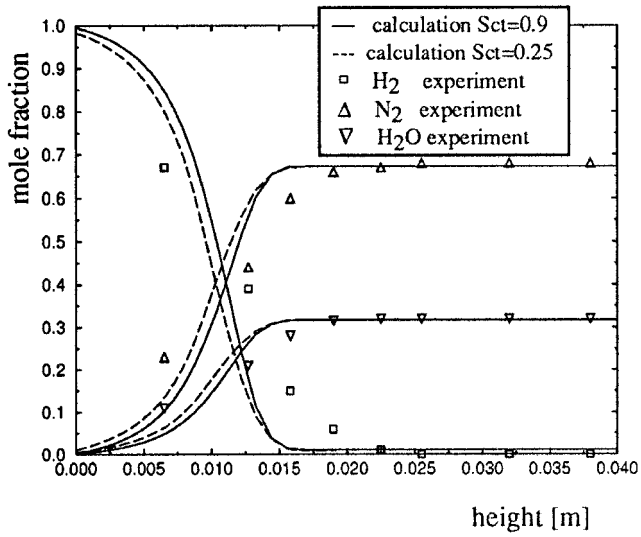

Fig. 6 Mole fraction profiles of H_2, N_2, and H_2O at x = 0.356 m.

Table 1 Boundary conditions for the Burrows and Kurkov[24] experiment

	Without combustion		With combustion	
	Mainstream	Injection	Mainstream	Injection
p, bar	1.0	1.0	1.0	1.0
T, K	1150	254	1270	254
Ma	2.44	1.0	2.44	1.0
Y_{H_2}	0.001	1.0	0.0	1.0
Y_{N_2}	0.766	0.0	0.486	0.0
Y_{O_2}	0.0	0.0	0.258	0.0
Y_{H_2O}	0.233	0.0	0.256	0.0
ϕ	——	——	0.27	——

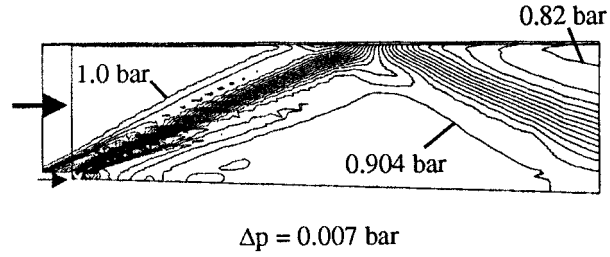

Fig. 7 Isolines of the pressure without combustion.

Table 2 Reaction scheme

Number	Reaction	B, mol, cm^3, s	n	E, kJ/mol
	H_2/O_2 chain reaction			
1f	$O_2 + H \rightarrow OH + O$	2.000E+14	0.00	70.30
1b	$OH + O \rightarrow O_2 + H$	1.568E+13	0.00	3.52
2f	$H_2 + O \rightarrow OH + H$	5.060E+04	2.67	26.30
2b	$OH + H \rightarrow H_2 + O$	2.222E+04	2.67	18.29
3f	$H_2 + OH \rightarrow H_2O + H$	1.000E+08	1.60	13.80
3b	$H_2O + H \rightarrow H_2 + OH$	4.312E+08	1.60	76.46
4f	$OH + OH \rightarrow H_2O + O$	1.500E+09	1.14	0.42
4b	$H_2O + O \rightarrow OH + OH$	1.473E+10	1.14	71.09
	HO_2 consumption and formation			
5f	$O_2 + H + M' \rightarrow HO_2 + M'$[a]	2.300E+18	−0.80	0.00
5b	$HO_2 + M' \rightarrow O_2 + H + M'$[a]	3.190E+18	−0.80	195.39
6	$HO_2 + H \rightarrow OH + OH$	1.500E+14	0.00	4.20
7	$HO_2 + H \rightarrow H_2 + O_2$	2.500E+13	0.00	2.90
8	$HO_2 + OH \rightarrow H_2O + O_2$	6.000E+13	0.00	0.00
9	$HO_2 + H \rightarrow H_2O + O$	3.000E+13	0.00	7.20
10	$HO_2 + O \rightarrow OH + O_2$	1.800E+13	0.00	−1.70
	H_2O_2 formation and consumption			
11	$HO_2 + HO_2 \rightarrow H_2O_2 + O_2$	2.500E+11	0.00	−5.20
12f	$OH + OH + M' \rightarrow H_2O_2 + M'$[a]	3.250E+22	−2.00	0.00
12b	$H_2O_2 + M' \rightarrow OH + OH + M'$[a]	1.692E+24	−2.00	202.29
13	$H_2O_2 + H \rightarrow H_2O + OH$	1.000E+13	0.00	15.00
14f	$H_2O_2 + H \rightarrow H_2 + HO_2$	1.700E+12	0.00	15.70
14b	$H_2 + HO_2 \rightarrow H_2O_2 + H$	1.150E+12	0.00	80.88
	Recombination reactions			
15	$H + H + M' \rightarrow H_2 + M'$[a]	1.800E+18	−1.00	0.00
16	$OH + H + M' \rightarrow H_2O + M'$[a]	2.200E+22	−2.00	0.00
17	$O + O + M' \rightarrow O_2 + M'$[a]	2.900E+17	−1.00	0.00

[a]Note: with $M' = 6.5[H_2O] + 0.4[O_2] + 0.4[N_2] + 1.0[\text{other}]$.

sponding pressure distribution. An expansion fan occurs at the injection step, followed by a shock wave. Because of the limited resolution of the grid in the middle of the channel, the pressure isolines are not perfectly smooth.

Two different reaction schemes were used for the simulation of the combustion. The first consists of one global reaction involving the four species: 1) hydrogen, 2) oxygen, 3) nitrogen, and 4) water. The reaction scheme is given by

$$2H_2 + O_2 \rightarrow 2H_2O$$

The activation energy was set to zero and the frequency factor was assumed to be very high [$B = 10^{18}$ cm^3/(mol s)]. The second consists of 17 elementary reactions with nine species (H, O, OH, H_2O, HO_2, H_2, O_2, H_2O_2, and N_2).[25] This reaction scheme is given in Table 2, where B denotes the frequency factor. Nitrogen is always considered as an inert species. Thus, three or eight additional species conservation equations have to be solved. Because the numerical scheme is implicit, matrices have to be solved. Thus, the number of equations quadratically influences the computational effort (CPU time and memory requirements). The complex reaction scheme is about four times slower than the single-step global model and needs about four weeks' computational time on an HP 715 workstation. The memory requirements for this model are about 6.3 Mbyte/1000 grid points. About 10,000 iterations were necessary to reach convergence with Courant–Friedrichs–Lewy numbers in the range between 5–10. The residual drop was usually on the order of four orders of magnitude. Furthermore, it was checked that the profiles did not change any more after 1000 additional iterations to ensure convergence.

Figures 8–10 show the profiles of the total temperature and four species H_2, O_2, N_2, and H_2O at the exit of the channel at $x = 356$ mm for the two reaction schemes. Comparison of the experimental data and the numerical results demonstrates the performance of the model. Only the temperature profile is shifted slightly toward the middle of the channel. The difference in the temperature peak between the two reaction schemes is because of the formation of the radicals, especially the H radical with its extremely high reference enthalpy. Figure 11 shows the mole fractions of the radicals H, OH, and O at the exit plane. Furthermore, small differences may be because of the fact that the one-step model does not include an ignition delay time. These differences are expected to increase with decreasing temperatures, because the ignition delay time increases.

There may be several reasons for the difference in the temperature and hydrogen mole fraction in the vicinity of the wall. Because of the probe diameter of 1 cm, experimental errors for the determination of the temperature close to the wall may not be ruled out. Another reason may be that the numerical method underestimates the diffusivity of the various species, as already mentioned. Nevertheless, the agreement between the experimental and numerical results for the mole fractions is quite satisfactory.

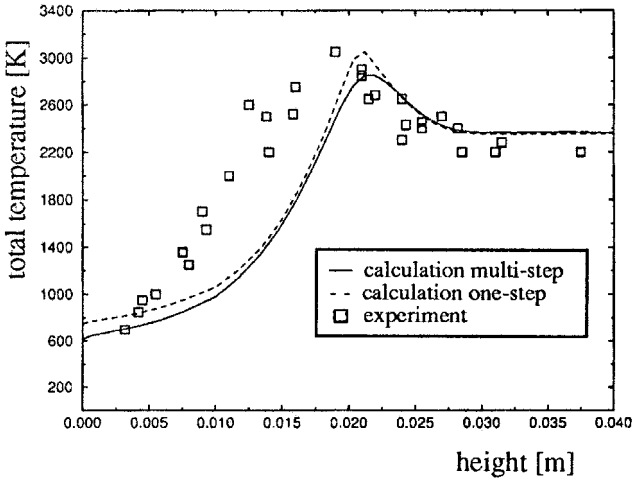

Fig. 8 Total temperature profile at $x = 0.356$ m.

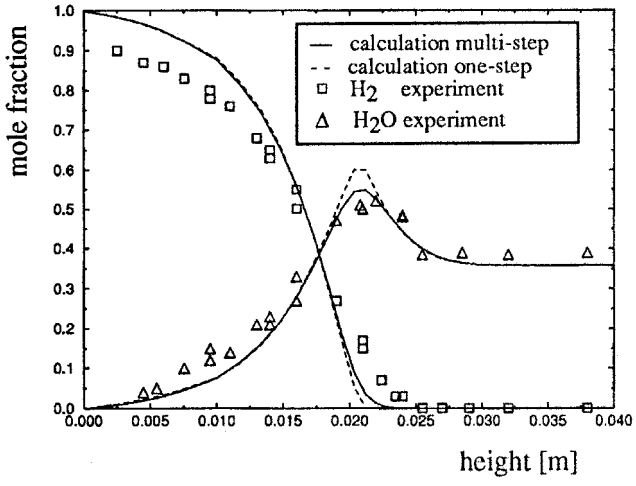

Fig. 9 Mole fraction profiles of H_2 and H_2O at $x = 0.356$ m.

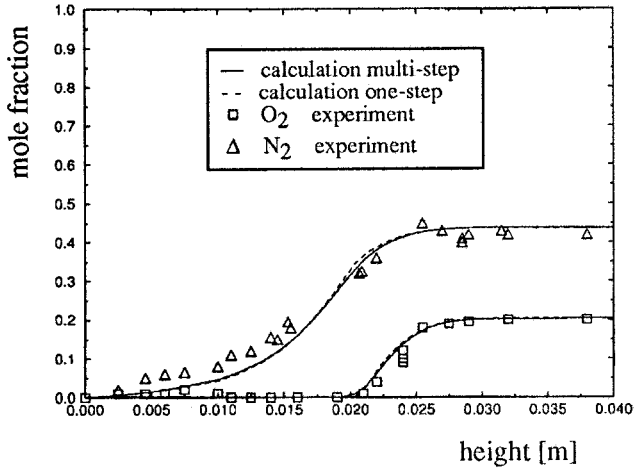

Fig. 10 Mole fraction profiles of N_2 and O_2 at $x = 0.356$ m.

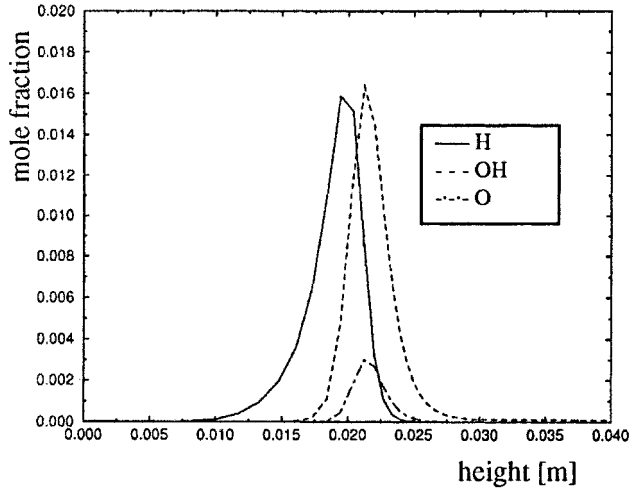

Fig. 11 Calculated mole fraction profiles of H, OH, and O at $x = 0.356$ m.

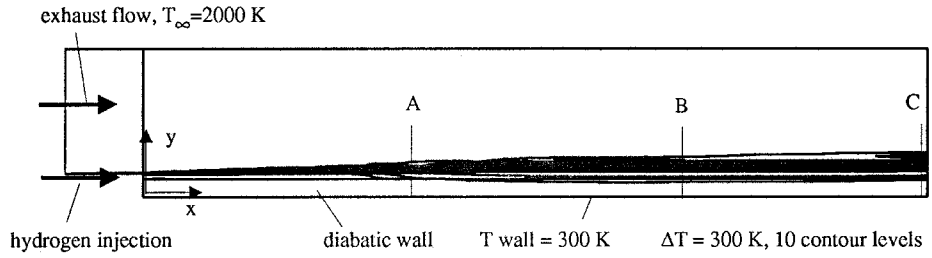

Fig. 12 Temperature distribution in the flow and wall regions.

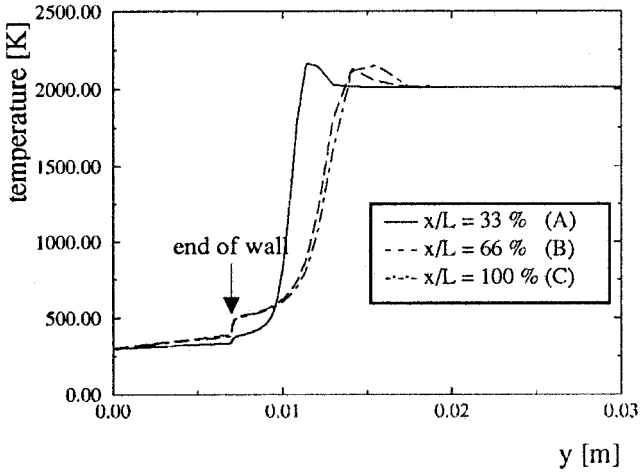

Fig. 13 Temperature profiles at different positions normal to the surface.

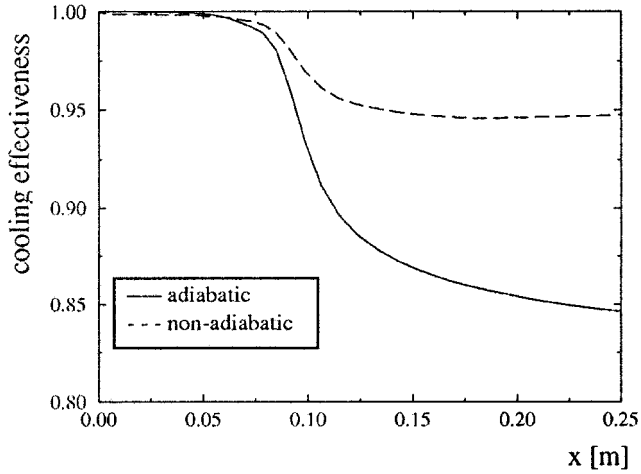

Fig. 14 Cooling effectiveness with adiabatic and nonadiabatic walls.

Film Cooling

Further simulations were performed to investigate the cooling effectiveness in a film-cooled nozzle, when hydrogen is injected parallel to an exhaust stream as a coolant. The exhaust stream has a temperature of 2000 K, a fuel-to-air ratio of 0.77, and a freestream velocity of 600 m/s, corresponding to a Mach number of 0.65. The injection temperature is 300 K. Because of the remaining oxygen in the exhaust flow, reaction of the oxygen with the hydrogen is to be expected. The simulations were performed with the global reaction scheme described earlier. To investigate the influence of nonadiabatic walls, the calculations were conducted with and without the solid-body block. In the first case, a constant temperature of 300 K was assumed on the lower side of the wall. This can be considered as convection cooling on the lower side.

Figure 12 shows the arrangement of the case and isolines of temperature in the case with a nonadiabatic wall. Because it is difficult to discern the temperature differences caused by the large gradients, temperature profiles are taken in the three sections A, B, and C. They are displayed in Fig. 13. It can be seen that the temperature gradient is quite small in the wall. It increases further downstream because of the higher heat conduction into the wall. Then, a steep gradient follows the temperature of the coolant. In the region of the coolant, the temperature gradient is again small, but then the temperature increases very rapidly in all three cases. The maximum temperature of about 2180 K is caused by the reactions taking place between hydrogen and oxygen. Finally, the freestream temperature is reached in the outer region. It can be observed that the gradient between coolant and main flow becomes less steep further downstream because of mixing and heat transfer, and that the maximum temperature is shifted upwards.

Figure 14 shows a comparison of the cooling effectiveness in the case with and without nonadiabatic walls. The cooling effectiveness is defined by

$$\eta_c = (T - T_\infty)/(T_c - T_\infty) \qquad (15)$$

where T is the temperature on the wall, and T_c is the temperature of the coolant. It can be seen that in the first 20% of the channel the cooling effectiveness is nearly equal to 100%, because the influence of the combustion has not reached the wall by means of heat transfer and mixing. But then a rapid decrease can be observed in both cases. While the cooling effectiveness reaches a constant value of about 95% in the case of the nonadiabatic wall, in the other case the effectiveness still decreases. Thus, a nonadiabatic wall with a constant temperature on the lower side significantly increases the cooling effectiveness of a film-cooled nozzle wall. It is surprising that even in spite of the reactions taking place between hydrogen and oxygen, the cooling effectiveness remains quite high, even far downstream of the injection slot. This may be because of the low mixing in the case of parallel injection. In the case of inclined injection, more rapid mixing and, thus, a decrease in cooling effectiveness is to be expected. At this point a more advanced turbulence model is desirable.

Conclusions

The extension of a numerical scheme for supersonic flows is presented in this paper; the scheme was originally developed for an ideal, nonreacting gas. It could be shown that the method employed for the modeling of the real-gas effects based on the equivalent ratio of specific heats also gives reasonable results for the mixing of different gases and for the supersonic combustion in a divergent channel. Furthermore, two different reaction models were employed for the simulation of the combustion. It could be shown that a simple model performs quite well, but that a more complex model including radicals is required to give more accurate results.

Investigations of a hydrogen film-cooled nozzle wall with parallel injection into an exhaust gas stream revealed that the cooling effectiveness remains quite high, even far downstream of the injection slot. The coupled calculations of fluid flow and nonadiabatic walls showed that the cooling effectiveness can be increased significantly by considering a nonadiabatic wall

with a constant temperature on the lower side. This approach to the simulation of convection- and film-cooled nozzle walls is very promising and gives more realistic temperature distributions than the assumption of adiabatic walls. Future work will concentrate on implementing two-equation turbulence models and more advanced coupling of turbulence and combustion.

References

[1]Yee, H. C., and Shinn, J. L., "Semi-Implicit and Fully Implicit Shock-Capturing Methods for Hyperbolic Conservation Laws with Stiff Source Terms," NASA TM-89415, Dec. 1986.

[2]Eklund, D. R., Hassan, H. A., and Drummond, J. P., "The Efficient Calculation of Chemically Reacting Flow," AIAA Paper 86-0563, Jan. 1986.

[3]Bussing, T. R. A., and Murman, E. M., "A Finite Volume Method for the Calculation of Compressible Chemically Reacting Flows," AIAA Paper 85-0331, Jan. 1985.

[4]Shuen, J.-S., and Yoon, S., "Numerical Study of Chemically Reacting Flows Using an LU Scheme," AIAA Paper 88-0436, Jan. 1988.

[5]Gerlinger, P., Algermissen, J., and Brüggemann, D., "Simulation of Turbulent Slot Injection of Different Gases into a Supersonic Air Stream," AIAA Paper 94-2247, June 1994.

[6]Pandey, A. K., Dechaumphai, P., and Wieting, A. R., "Thermal-Structural Finite Element Analysis Using Linear Flux Formulation," AIAA Paper 89-1224, April 1989.

[7]Ramakrishnan, R., Kim, S. B., and Thornton, E. A., "Adaptive Quadrilateral and Triangular Finite-Element Scheme for Compressible Flows," *AIAA Journal*, Vol. 28, No. 1, 1990, pp. 51–59.

[8]Heselhaus, A., Vogel, D. T., and Krain, H., "Coupling of 3D-Navier-Stokes External Flow Calculations and Internal 3D-Heat Conduction Calculations for Cooled Turbine Blades," *Heat Transfer and Cooling in Gas Turbines*, CP-527, AGARD, 1992.

[9]Heselhaus, A., and Vogel, D. T., "Numerical Simulation of Turbine Blade Cooling with Respect to Blade Heat Conduction and Inlet Temperature Profiles," AIAA Paper 95-3041, July 1995.

[10]Kee, R. J., Dixon-Lewis, G., Warnatz, J., Coltrin, M. E., and Miller, J. A., "A Fortran Computer Code Package for the Evaluation of Gas-Phase Multicomponent Transport Properties," Sandia National Labs., Rept. 86-8246, March 1994.

[11]Godunov, S. K., "A Finite-Difference Method for the Numerical Computation of Discontinuous Solutions of the Equations of Fluid Dynamics," *Matematicheskii Sbornik*, Vol. 47, 1959, pp. 271–290.

[12]Anderson, W. K., Thomas, J. L., and Van Leer, B., "A Comparison of Finite Volume Flux Vector Splittings for the Euler Equations," AIAA Paper 85-0122, Jan. 1985.

[13]Eberle, A., Schmatz, M. A., and Bissinger, N., "Generalized Flux-vectors for Hypersonic Shock-Capturing," AIAA Paper 90-0390, Jan. 1990.

[14]Eberle, A., "Characteristic Flux Averaging Approach to the Solution of Euler's Equations," Lecture Series 4, Computational Fluid Dynamics at VKI, Parts I and II, March 1987.

[15]Eberle, A., "Numerische Elemente für DEMONSTRATOR-Nachrechnungen mit einem neuen EULER-Verfahren," Messerschmitt-Bölkow-Blohm, UFE-AERO-MT-832, Munich, Germany, March, 1989.

[16]Schmatz, M. A., "Hypersonic Three-Dimensional Navier-Stokes Calculations for Equilibrium Gas," AIAA Paper 89-2183, July 1989.

[17]Baldwin, B. S., and Lomax, H., "Thin Layer Approximation and Algebraic Model for Separated Turbulent Flows," AIAA Paper 78-257, Jan. 1978.

[18]Metz, S., "Numerische Verfahren zur Berechnung des Stoff- und Impulstransports in H_2/Luft. und CH_4/Luft-Gemischen," Ph.D. Dissertation, Aachen Univ. of Technology, Aachen, Germany, 1995.

[19]Aretz, W., Metz, S. W., Wilhelmi, H., Joly, V., Coquel, F., and Marmignon, C., "A General and Consistent Model for Transport and Relaxation in Chemical and Thermodynamic Nonequilibrium Applied to a 5-Component Air Reentry Flow," AIAA Paper 93-5115, Dec. 1993.

[20]Bohn, D., Bonhoff, B., Lang, G., and Schönenborn, H., "Validation of a Numerical Model for the Coupled Simulation of Fluid Flow and Diabatic Walls with Application to Film-Cooled Gas Turbine Blades," Verein Deutscher Ingenieure-Berichte Nr. 1186, Erlangen, March 1995.

[21]Bohn, D., Bonhoff, B., Lang, G., and Schönenborn, H., "Determination of Thermal Stress and Strain Based on a Combined Aerodynamic and Thermal Analysis for a Turbine Nozzle Guide Vane," American Society of Mechanical Engineers, Paper 95-CTP-89, Aug. 1995.

[22]Hansmann, T., Wilhelmi, H., and Bohn, D., "An Experimental Investigation of the Film-Cooling Process at High Temperatures and Velocities," AIAA Paper 93-5062, Nov. 1993.

[23]Libby, P. A., and Williams, F. A., *Turbulent Reacting Flows*, Springer–Verlag, Berlin–Heidelberg, 1980, p. 5.

[24]Burrows, M. C., and Kurkov, A. P., "Supersonic Combustion of Hydrogen in a Vitiated Air Stream Using Stepped-Wall Injection," AIAA Paper 71-721, June 1971.

[25]Peters, N., and Rogg, B., *Reduced Kinetic Mechanisms for Applications in Combustion Systems*, Springer–Verlag, Berlin–Heidelberg, 1993.